A numerical study of the effect of surface tension and noise on an expanding Hele–Shaw bubble

Wei-Shen Dai
The James Franck Institute, The University of Chicago, 5640 South Ellis Avenue, Chicago, Illinois 60637

Michael J. Shelley
Computational and Applied Mathematics Program, Ryerson Laboratory, The University of Chicago, Chicago, Illinois 60637

In this paper, the dynamics of an interface under the influence of surface tension is studied numerically for flow in the Hele–Shaw cell, where the interface separates an expanding bubble of inviscid fluid from a displaced viscous fluid. Of special interest is the long–time behavior of the so-called q-pole initial data, whose motion is explicitly known and globally smooth for the zero surface tension flow. The numerical method is spectrally accurate and based upon a boundary integral formulation of the problem, together with a special choice for the frame of motion along the interface. In 64-bit arithmetic, a transition from the formation of side branches to tip splitting is observed as the surface tension is decreased. The tip splitting occurs on a time scale that decreases with the surface tension. This is consistent with some experimental observations. However, by increasing the arithmetic precision to 128 bits, it is found that this transition occurs at a yet smaller surface tension. The tip splitting is associated with the growth of noise in the calculation at unstable scales allowed by the surface tension, and a simple linear model of this growth seems to agree well with the observed behavior. The robustness of the various observed structures to varying amounts of noise is also investigated numerically. It is found that the appearance of side branches seems to be the intrinsic effect of surface tension, and the time scales for their appearance increases as the surface tension decreases. These results suggest, with some qualification, that surface tension acts as a regular perturbation to evolution from this initial data, even for long times.

I. INTRODUCTION

Fluid flow in the Hele–Shaw cell is quasi-two-dimensional because the fluids involved are confined between two closely spaced plates. The case in which one fluid (usually with a negligible viscosity) displaces another has been studied extensively. Exact, self-similar shapes (the Saffman–Taylor fingers) have been found for the interface between the two fluids, when surface tension is absent, for the channel geometry.[1,2] Much of the subsequent work is concerned with the role of surface tension along the interface in the selection of finger width (see Ref. 3 for a review). More recent experimental and theoretical work considered self-similar solutions and the role of surface tension in circular or sector geometries.[4–8] Increasingly, interest has been drawn to another aspect of the problem—time-dependent behavior. The complex patterns formed by an expanding bubble are striking (for some of the experiments, see Refs. 9–11). Natural questions concern the role of surface tension, as well as its interaction with noise, in producing these structures. Certain initial conditions with simple analytic strucure are particularly interesting. In these cases, the time-dependent behavior under zero surface tension is governed by a set of ordinary differential equations, and in this sense, the flows are exactly solvable[12–15] (or see Ref. 16 for a brief review). Some asymptotic analyses have also been done to see how these solutions, most especially their analytic structures, change in the presence of small surface tension.[17–20]

Recently, for such initial data that give expanding inviscid bubbles, Dai, Kadanoff, and Zhou[16] (subsequently referred to as DKZ) performed a numerical study of their evolution under surface tension. In the absence of surface tension, these initial conditions give bubble interfaces that form outward cusps at a finite time (the q-zero data), as well as bubble interfaces with broad expanding "petals," that exist and remain smooth for all time (the q-pole data). By this property these latter solutions most resemble the Saffman–Taylor fingers. The computational method used by DKZ was based on conformal mapping. For the q-zero data with surface tension, they observed that the interface remained smooth, and the cusp was replaced by a bulb of fluid. For the q-pole initial condition, the computational approach limited their study to the early time behavior of the interface shape, and little difference was observed in the shape of the interface with a small surface tension as compared to that without.

The q-pole data is a good vehicle through which to investigate the effect of small surface tension over long times. The underlying zero surface tension solution is explicitly known and nontrivial, and exists for all time, but is not an exact solution in the presence of surface tension (unlike an expanding circle). And the limit of zero surface tension is an interesting one here. The interface problem with zero surface tension is linearly ill-posed, and singularity formation seems generic for the system. Therefore, it is not clear that surface tension acts as a regular perturba-

tion for arbitrarily long times even when the underlying solution exists and is smooth.

In this paper, we study numerically the longer time behavior of the q-pole initial data. Instead of a conformal mapping method, we employ a boundary integral method in which the interface is represented as a vortex sheet. The vortex sheet strength satisfies a Fredholm integral equation of the second kind, and with the appropriate quadrature method, the resulting set of linear equations can be solved rapidly through iteration. This method is spectrally accurate and with special choices for the frame of motion of computational points along the interface, it is successful in solving the long-time behavior of the Hele–Shaw flow.

Calculating in 64-bit arithmetic, we find that at "large" surface tensions the interface rapidly forms a nearly circular shape. As the surface tension is decreased, the computed solution resembles more closely the zero surface tension solution, and the effect of surface tension is to create side-branch structures on the interface. As the surface tension is decreased yet further, a transition is observed to tip splitting, which occurs on a time scale that decreases with the surface tension. This is consistent with some experimental evidence.[21] However, by increasing the arithmetic precision to 128 bits, we find that this transition occurs at a yet smaller surface tension, and we associate the tip splitting with the growth of noise in the calculation at unstable scales allowed by the surface tension. A simple linear model of this growth seems to agree well with the observed behavior. Through investigating numerically the robustness of the various observed structures to varying amounts of noise, we conclude that the appearance of side branches seems to be the intrinsic effect of surface tension. The time scales for the appearance of the side-branching structures increase as the surface tension decreases, which suggests that for our initial condition, surface tension acts as a regular perturbation even for long times. Qualifications to this statement are discussed below.

This approach is similar to studies carried out in the study of vortex sheet motion in two-dimensional Eulerian fluids. There the linear motion is ill-posed due to the Kelvin–Helmholtz instability. Krasny[22] regularized the motion by smoothing the Birkhoff–Rott integral, and noted the interplay between the smoothing parameter and the precision of the calculation. Baker and Shelley,[23] replacing the sheet with a thin layer of constant vorticity, reached a similar conclusion.

The organization of this paper is as follows. The boundary integral formulation of the problem is given in Sec. II. The numerical methods for solving this formulation are discussed in Sec. III. In Sec. IV, the particular initial conditions of interest and their evolution under zero surface tension are described. Numerical calculations of an interface under zero surface tension are discussed in Sec. V. In Sec. VI, simulational results for several surface tension parameters are presented and their dependence on noise and surface tension is analyzed. Some concluding remarks are given in Sec. VII.
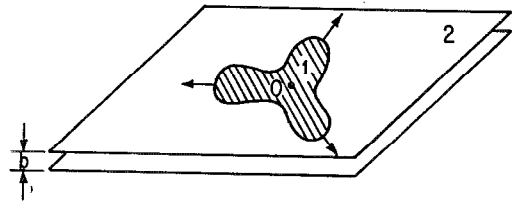

FIG. 1. The Hele–Shaw cell. Fluid 1 and fluid 2 are confined between two plates separated by a distance b. A bubble containing fluid 1, which has negligible viscosity, expands into fluid 2.

II. THE BOUNDARY INTEGRAL FORMULATION OF THE EQUATIONS OF MOTION

Boundary integral methods have been used to compute free surface motion of inviscid and incompressible fluids (see, for example, Ref. 24). Tryggvason and Aref used such methods to find the time-dependent behavior of Hele–Shaw flow in a channel geometry with periodic boundary conditions.[25] There, a boundary integral representation was used to obtain the vorticity density on the free interface, and vortex-in-cell techniques were then used to evolve the interface. In this paper, a similar formulation is used, but the interface is evolved with its velocity derived directly from the integral representation. The formulation here is closer to that used by DeGregoria and Schwartz to solve the evolution in a channel geometry.[26,27] Since in our problem, the periodic boundary condition arises naturally from the closed smooth interface, the quadrature methods used for the boundary integrals give a spectrally accurate evolution in space.

Here we are interested in Hele–Shaw flow in a circular geometry. The spacing between the two closely spaced plates is b. We assume fluid 1 has a negligible viscosity, while fluid 2 has a finite viscosity μ and is incompressible. As shown in Fig. 1, fluid 1 forms a bubble inside fluid 2. Fluid 1 is kept at constant pressure and mass is being pumped through point O at a constant rate. So its area S increases at a constant rate dS/dt. The region occupied by fluid 2 is the physical region and we are interested in obtaining the time-dependent behavior of the interface between the two fluids. Once the interface is known, we can calculate all the physical quantities of fluid 2.

In fluid 2, we have Darcy's law:

$$\mathbf{v} = -\frac{b^2}{12\mu} \nabla P, \tag{1}$$

together with the incompressibility constraint

$$\nabla \cdot \mathbf{v} = 0, \tag{2}$$

where $\mathbf{v}$ and P are the velocity and pressure, respectively, of fluid 2. Thus, the pressure is harmonic and plays the role of a velocity potential, and the velocity field is irrotational.

There are boundary conditions on the velocity. At infinity there is the contribution from the mass source at point O. At large distances, the increase in area of fluid 1 produces a radial velocity inversely proportional to the distance from the injection point:

$$\mathbf{v}(\mathbf{x}) \overset{|\mathbf{x}| \to \infty}{\longrightarrow} \frac{1}{2\pi} \frac{dS}{dt} \frac{\mathbf{x}}{|\mathbf{x}|^2}, \tag{3}$$

where dS/dt is the time derivative of the area of the bubble. On the interface there is the Laplace–Young condition:

$$P|_{\text{interface}} = \tau \kappa, \tag{4}$$

where τ is the surface tension and κ is the local curvature. Using Eq. (1) on the interface, this can be rewritten as the boundary condition on the velocity:

$$\mathbf{s} \cdot \mathbf{v} = -\frac{b^2}{12\mu} P_s = -\frac{S_t}{2\pi} d_0 \kappa_s. \tag{5}$$

Here $\mathbf{s}$ is the unit tangent to the interface, the subscript s denotes differentiation with respect to the arclength, and $d_0 = 2\pi\tau b^2/12\mu S_t$ is an amalgamated surface tension parameter with units of length (as in DKZ). There is the further physical requirement that the interface move with the fluid. We will now see that the motion of the interface completely determines the motion of the fluid.

The description of fluid 2 is put into a convenient form by using complex variables. Let $Q^* = u - iv$ be the complex conjugate velocity field, $\eta = x + iy$ a point in fluid 2, and $z(p) = x(p) + iy(p)$ a 2π-periodic function in a real parameter p, which describes the location of the closed interface. Following Tryggvason and Aref,[25] we can write the velocity as the sum of two contributions:

$$Q^*|_\eta = \frac{dS/dt}{2\pi} \frac{1}{\eta} + \frac{1}{2\pi i} \int_0^{2\pi} \frac{\gamma(p')}{\eta - z(p')} dp'. \tag{6}$$

The second term is an irrotational velocity, given as a vortex sheet along the interface, with vortex sheet strength $\gamma(p)$. The first term is the velocity induced by the pumping at O. The boundary condition equation (3) is satisfied by the first term since for large η the integral term contributes only at $O(1/\eta^2)$, not $O(1/\eta)$, because $\gamma(p)$ has zero mean (see below). The boundary condition (5) is satisfied through the determination of the vortex sheet strength. Using the Plemelj formula to take the limit of Eq. (6) to the interface, we have

$$\lim_{\eta \to z(p)} Q^*|_\eta = \frac{dS/dt}{2\pi} \frac{1}{z(p)} + \frac{1}{2} \frac{\gamma(p)}{z_p(p)}$$

$$+ \frac{1}{2\pi i} P \int_0^{2\pi} \frac{\gamma(p')}{z(p) - z(p')} dp'. \tag{7}$$

Here $P\int$ denotes the principal value integral and the subscripts indicate partial derivatives. The integral in Eq. (7) is called the Birkhoff–Rott integral.

Using Eq. (7) together with boundary condition equation (5), the following integral equation is found easily for $\gamma(p)$:

$$\gamma(p) = -2 \operatorname{Re}\left(z_p(p) \frac{1}{2\pi i} P \int_0^{2\pi} \frac{\gamma(p')}{z(p) - z(p')} dp' \right)$$

$$- 2d_0 \kappa_p(p) - 2 \operatorname{Re}\left(\frac{dS/dt}{2\pi} \frac{z_p(p)}{z(p)} \right). \tag{8}$$

Finally, we enforce the requirement that the interface move with the fluid through the evolution equation

$$\frac{\partial z^*}{\partial t}(p,t) = \left(\frac{1}{z(p)} + \frac{1}{2} \frac{\gamma(p)}{z_p(p)} + \frac{1}{2\pi i} P \int_0^{2\pi} \frac{\gamma(p')}{z(p) - z(p')} dp' \right)$$

$$+ T(p) \frac{z_p^*(p)}{s_p(p)}, \tag{9}$$

where $s_p(p) = |z_p(p)|$ is the derivative of the arclength with respect to p. As in Refs. 15 and 16, S_t is set hereafter to 2π. The term in parentheses is simply the fluid velocity evaluated at the interface. The remaining term is a velocity in the direction tangent to the interface, and corresponds to a choice for the frame of motion of points along the interface which comes from a specific parametrization of the curve. For example, if $T \equiv 0$, then a point on the interface moves in the Lagrangian (fluid) frame. This change-of-frame term is included for computational convenience, and specific choices for T will be discussed in the following sections. Aside from the inclusion of a change-of-frame term, the only change in Eqs. (8) and (9) from those given in Ref. 25 is that the pumping term replaces a gravitational term.

Equations (8) and (9) constitute a complete formulation of the interface evolution problem. Equation (8) is a Fredholm integral equation of the second kind for $\gamma(p)$. It is known that Eq. (8) has a unique solution, which can be found through fixed point iteration (see, for example, Ref. 28). We write Eq. (8) as

$$\gamma(p) = L(\gamma)(p) + \theta_p(p), \tag{10}$$

where L is the linear integral operator in Eq. (8), and θ_p are those terms not involving γ and are a perfect derivative in p. This implies that γ has zero mean, and thus is also a perfect derivative. The eigenvalues λ of L are real, have multiplicity one, and satisfy $|\lambda| \leq 1$.[28] In particular, $\lambda = -1$ is an eigenvalue while $\lambda = +1$ is not. The eigenvector associated with eigenvalue -1 has a nonzero mean. In the above equation, both $\gamma(p)$ and $\theta_p(p)$ have zero mean, thus the eigenvalue -1 is not relevant to any fixed point iteration whose beginning iterate has zero mean, and the iteration will converge to the solution of Eq. (10). For use in the next section, we also note that for the adjoint linear operator of L, any constant is the eigenfunction associated with $\lambda = -1$.

The result of linear analysis of an expanding circular bubble of radius $R(t)$ provides an instantaneous growth rate $\sigma_k(t)$ for a perturbation of wave number $k > 0$. This growth rate in the analytic frame is (see, for example, Ref. 15):

$$\sigma_k(t) = \frac{1}{R(t)^2} \left((k-1) \frac{dS/dt}{2\pi} - \frac{d_0}{R(t)} (k-1)k(k+1) \right). \tag{11}$$

For a constant pumping rate, say $dS/dt = 2\pi$, we obtain the familiar Mullins–Sekerka instability, seen in many other contexts,[29] which shows the competition between the destabilization effect due to pumping and the stabilizing effect due to surface tension. For $d_0 = 0$, σ_k scales with k, and the

system is linearly ill-posed (the growth rates are unbounded for $k \to \infty$). This is very similar to the linearized behavior associated with the Kelvin–Helmholtz instability of Eulerian fluid dynamics. When d_0 is positive, the surface tension stabilizes the high modes, and for d_0 sufficiently small, there is a mode of maximum growth, whose wave number scales roughly with the surface tension as $d_0^{-1/2}$. Note also that the "effective surface tension," $d_0/R(t)$, decreases as the size of the bubble increases.

III. NUMERICAL METHODS

Here we discuss the numerical discretization and solution of Eqs. (8) and (9). The use of an alternate-point quadrature method gives spectral accuracy in calculating the principal value integrals,[30,31] and spatial derivatives are also found with spectral accuracy through the discrete Fourier transform (DFT). As in calculations of the Kelvin–Helmholtz instability by Krasny,[32] we filter the interface in Fourier space at each time step. The convergence of such a scheme for Hele–Shaw flow has been subsequently proved, both with or without surface tension.[33,34]

Assuming that the interface is a closed curve, then $z(p)$ and $\gamma(p)$ are 2π-periodic functions of p. The interval $[0,2\pi)$ in p is discretized uniformly with $p_j = jh$, for $j = 0,1,...,N-1$ and $h = 2\pi/N$. An integer subscript denotes position, and by $z_j(t)$ is meant an approximation to $z(jh,t)$ (and likewise for γ_j, etc.). By $z_j'(t)$ is meant a discrete approximation to $z_p(jh,t)$.

The choice of a quadrature method for the Birkhoff–Rott integral in Eq. (9), together with a method of differentiation in p, determines the discretized linear system to be solved for γ_j. Here the Birkhoff–Rott integral is discretized by the modified point vortex approximation (MPVA) to yield for Eq. (9) the system of ordinary differential equations (ODE's)

$$z_j^*(t) = \frac{1}{z_j} + \frac{1}{2}\frac{\gamma_j}{z_j'} + \frac{2h}{2\pi i}\sum_{\substack{k=0 \\ j+k \text{ odd}}}^{N-1}\frac{\gamma_k}{z_j - z_k} + T_j\frac{z_j'^*}{s_j'}, \quad (12)$$

for $j = 0,1,...,N-1$. When $z(p)$ and $\gamma(p)$ are analytic functions of p, the MPVA is an infinite-order approximation to the Birkhoff–Rott integral. In particular, if both γ and z are analytic on the strip $[-i\rho, +i\rho]$ for $\rho > 0$, it can be shown that the discretization error of the MPVA to the Birkhoff–Rott integral can be bounded by a term of the form $C(\rho)e^{-\rho N}$ (see Ref. 31).

The discretized form of Eq. (8) is then

$$\gamma_j = -2 \operatorname{Re}\left(z_j'\frac{2h}{2\pi i}\sum_{\substack{k=0 \\ j+k \text{ odd}}}^{N-1}\frac{\gamma_k}{z_j - z_k}\right) + \theta_j'. \quad (13)$$

We find that when the interface is well resolved, Eq. (13), like Eq. (10), is contractive and can be solved by fixed point iteration at each time step. However, the discretization introduces its own complications. For convenience we write the fixed point iteration of Eq. (13) in matrix notation as

$$\Gamma^{n+1} = L_h\Gamma^n + \Theta', \quad (14)$$

and make several remarks.

(1) The iteration matrix L_h is such that elements of Γ with even index are only updated by elements of Γ with odd index, and vice versa. This has several consequences. First, if λ is an eigenvalue of L_h then so is $-\lambda$; L_h has a discrete eigenvalue very close to -1, the continuous eigenvalue of L. As it will be exponentially close when N is large, let us assume that it is -1. Thus L_h has an eigenvalue of $+1$ which arises solely from the discretization, and the Fredholm alternative must now be satisfied for invertibility. That is, for invertibility it is required that $W_1 \cdot \Theta' = 0$ where W_1 is the eigenvector of the adjoint operator L_h^T associated with $\lambda = 1$. This brings in the second consequence of the odd/even structure of L_h. If $V_\lambda = \{v_j\}$ is the eigenvector associated with λ, then $V_{-\lambda} = \{(-1)^j v_j\}$. Fortunately, L_h^T inherits the odd/even structure of L_h. Again, dropping terms exponentially small in N, the eigenvector $W_{-1} = \{w_j\}$ of L_h^T satisfies $w_j = 1$, and thus $W_1 = \{(-1)^j\}$. This is the DFT basis vector at the Nyquist frequency $N/2$. The solvability condition then becomes simply that Θ' has no component in its DFT at this frequency. This is achieved by either explicitly setting the $N/2$ mode to zero, or by the interface being well resolved in which case the highest frequencies are of the size of the round-off.

(2) The odd/even structure of the iteration matrix also implies that the iteration matrix L_h has Property A (see, for example, Ref. 35, p. 121). Such iteration matrices appear in solving other elliptical problems using finite-difference methods, and schemes for accelerating the convergence of the Jacobi (fixed point) iteration have been discovered and analyzed.[35] Here we use the cyclic Chebyshev semi-iterative method which requires ten times fewer iterations than the Jacobi method.

(3) Other spectrally accurate discretizations of the integral equation (8), related to Eq. (13), can be found and analyzed. Making use of the following identity,

$$\frac{1}{2\pi i} P \int_0^{2\pi} \frac{z_p(p')}{z(p) - z(p')} dp' + \frac{1}{2} = 0,$$

Eq. (8) can be rewritten as

$$\gamma(p) = -2 \operatorname{Re}\left(\frac{1}{2\pi i} P \int_0^{2\pi} \frac{z_p(p)\gamma(p') - z_p(p')\gamma(p)}{z(p) - z(p')}\right.$$
$$\left. \times dp' - \frac{1}{2}\gamma(p)\right) + \theta_p(p).$$

Note that the integrand is now smooth. Applying the MPVA to this form of Eq. (8) yields the matrix equation

$$\Gamma = (L_h + D_h)\Gamma + \Theta',$$

where the diagonal matrix D_h arises from the MPVA to the identity above. Each component of D_h is thus exponentially small in N. This yields naturally the two matrix iterations

$$\Gamma^{n+1} = (L_h + D_h)\Gamma^n + \Theta' \quad \text{or} \quad (I - D_h)\Gamma^{n+1} = L_h\Gamma^n + \Theta'.$$

In the first, $+1$ is an exact eigenvalue of the iteration matrix (no exponentially small terms), and the associated, exact eigenvector to the transposed operator is $W_1 = \{(-1)^j\}$. However, the iteration matrix is no longer of Property A. The iteration matrix of the second method is of Property A, and now has both ± 1 as exact eigenvalues. But, as with Eq. (13), the identity $W_1 = \{(-1)^j\}$ only holds to exponentially small terms in N.

(4) Each time step involves direct evaluations of the Birkhoff–Rott integral at a computational complexity of $O(N^2)$. While not cost effective for the values of N used here, at larger values of N it would be worthwhile to employ a fast summation method, such as the method of local corrections[36] or a fast multipole method.[37]

After solving Eq. (13) to obtain γ_i, the velocity of the interface is calculated through Eq. (12). The evolution is advanced by a fourth-order Runge–Kutta routine. To maintain resolution of the interface, the number of points is doubled (using the DFT) whenever the highest Fourier modes of the interface begin to rise out of the round-off. For zero and small surface tension calculations it is necessary to filter the solution to control the anomalous amplification of round-off error.[32] This is due to the ill-posedness of the linearized motion, as indicated by the dispersion relation (11). The filter is accomplished at the level of the round-off of the calculation. At each time step the DFT of $z(p)$ is formed. If a Fourier amplitude is less than a prescribed tolerance, it is set to zero. For example, in our 64-bit (15 digits) and 128-bit (30 digits), this tolerance is set to 10^{-12} and 10^{-26}, respectively.

IV. INITIAL CONDITIONS AND THEIR EVOLUTION UNDER ZERO SURFACE TENSION

We follow DKZ by focusing on initial datum for which the exact evolution is known when the surface tension is zero. The exact motion is nontrivial, and a review of these results (see also Refs. 12–15) is given in DKZ. We consider two particular examples of such initial data. In the first, the initially smooth interface sharpens outwards and loses its smoothness at a finite time by the formation of a cusp. In the second, the motion of the expanding interface exists for all time, and bears some resemblance to experimentally observed bubbles.

In the results presented hereafter, the initial interface has a q-fold symmetry which is preserved by the equations of motion. This symmetry is incorporated into the algorithm, and N refers now to the number of points resolving this portion of the interface. The Fourier expansion of $z(p)$ then has the form:

$$z(p) = e^{ip} \sum_{n=-\infty}^{+\infty} a_n e^{iqnp}.$$

Following DKZ the "q-zero" initial condition refers to the q-fold symmetric initial shapes of the interface,

$$z(p, t=0) = e^{ip}\left(1 - \frac{u_0}{(1-q)} e^{-iqp}\right), \qquad (15)$$

where, $u_0 \epsilon (0,1)$. This is a map from the unit circle onto the interface if p is considered to be the angle on the unit circle. By substituting ω for e^{ip} with $|\omega| \geqslant 1$, the resulting map, $f(\omega)$, maps the unit circle and its exterior analytically onto the whole physical domain; $f(\omega)$ is the Riemann map of the physical region.[38] The map preserves this distribution of zeros and evolves as

$$f(\omega) = A(t)\omega\left(1 - \frac{u(t)}{(1-q)\omega^q}\right), \qquad (16)$$

where the real functions $A(t)$ and $u(t)$ satisfy a coupled pair of ODE's, and have initial values $A(0) = 1.0$ and $u(0) = u_0 < 1$. For $q \geqslant 3$, $A(t)$ and $u(t)$ are monotonically increasing functions of time. There is a critical time t_c, at which $u=1$, and the derivative, $g=f_\omega$, acquires a zero on the unit circle. Consequentially, the interface develops cusps and the solutions break down (see Ref. 12). For $q=3$ and $u_0 = 0.5$, the critical time is $t_c = 0.5625\ldots$.

Conversely, there are also initial conditions for which the motion exists for all time. The "q-pole" initial condition refers to the q-fold symmetric initial shapes of the interface,

$$z(p, t=0) = e^{ip} \sum_{n=-\infty}^{0} \frac{u_0^{-n}}{1+qn} e^{iqnp}, \qquad (17)$$

where $u_0 \epsilon (0,1)$. Again, a Riemann map of the physical region is given by replacing e^{ip} in (17) with ω for $|\omega| \geqslant 1$. The evolution is as follows:

$$z(p,t) = A(t)\frac{v(t)}{u(t)} e^{ip} + A(t)e^{ip} \sum_{n=-\infty}^{0} \frac{u^{-n}(t)}{(1+qn)}$$
$$\times \left(1 - \frac{v(t)}{u(t)}\right) e^{inqp}, \qquad (18)$$

where $A(t)$, $v(t)$, and $u(t)$ are real functions whose evolution is governed by a set of ODE's. Here g has as singularities q simple poles, at $\omega = u(t)^{1/q} e^{i2\pi m/q}$, and also q simple zeros, at $\omega = v(t)^{1/q} e^{i2\pi m/q}$ for $m = 0(1)(q-1)$, all within the unit circle. The time evolution of the conformal map preserves this distribution of poles and zeros in g (see Ref. 16). By choosing the initial conditions $A(0)=1$, $v(0)=0$, and $u(0)=u_0 > -0$, we have that $0 < v(t) < u(t) < 1$ for all $t > 0$. That is, the solution always exists. Moreover, both $v(t)$ and $u(t)$ approach 1 for large times (u exponentially, and v algebraically).

The variable p above is not the Lagrangian variable that one obtains by setting $T \equiv 0$ in Eq. (9) but rather the parametrization which yields the Riemann map, when the substitution $f(\omega = e^{ip}) = z(p)$ is made. In Eq. (9), this parametrization corresponds to a specific choice of T, given in the Appendix. We refer to this choice as the analytic frame. That both of these initial conditions evolve without the introduction of any high wave-number component for $n \geqslant 1$ reflects the fact that the singularities of g are within the unit circle.
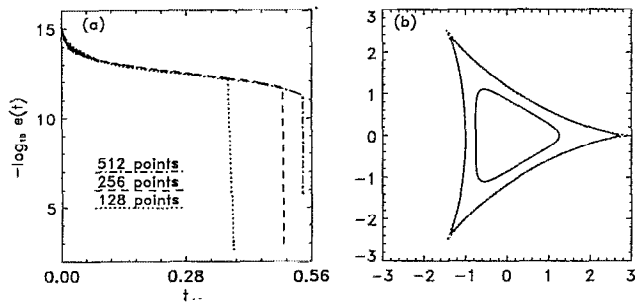
FIG. 2. Results for the three-zero initial condition (15) under zero surface tension with $u_0=0.5$. (a) $-\log_{10}[e(t)]$ vs t, where $e(t)$ is the maximum deviation of the result of calculation in the analytic frame from the exact solution. The three curves are for $N=128$, 256, and 512. The critical time for cusp formation is $t_c=0.5625\ldots$. (b) Simulational results for the expanding interface with $N=512$ at $t=0.0$ and 0.54. The dashed curve is the exact solution at $t=0.56$.
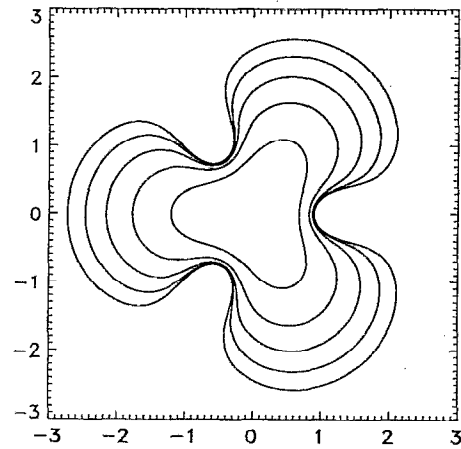

FIG. 3. Simulational results for the expanding interface from three-pole initial condition (17) with $N=256$. The initial condition is $u_0=0.5$. The times for the shapes (moving from inside out) are 0.0, 0.5, 1.0, 1.5, and 2.0.

V. CALCULATIONS WITH ZERO SURFACE TENSION

In this section, we present numerical calculations for both the q-zero and q-pole initial conditions. We examine the robustness of the method, and illustrate the very strong effect the choice of frame has upon the accuracy of the calculation. When the surface tension is zero, we find that the choice of a good frame in which to compute varies from problem to problem.

We consider first the q-zero initial condition, with $q=3$ and $u_0=0.5$. Then there is critical time, $t_c \approx 0.5625$, when the interface develops a cusp. Equations (8) and (9) were solved in the Lagrangian frame [$T(p)\equiv0$], with $N=128$ and $\Delta t=10^{-4}$. By $t=0.1$, well before t_c, the highest Fourier modes had exceeded the round-off. While there are but two modes in the analytic frame, a full spectrum develops in the Lagrangian frame.

Following Ref. 15, in the Appendix is given an expression for $T(p)$ [Eq. (A5)], which retains the points in the analytic frame. Equations (8) and (9) were solved with this $T(p)$ and the initial data above. Three calculations with $N=128$, 256, and 512, respectively, were carried out until the iteration of Eq. (8) stopped converging. For each calculation, $\Delta t=10^{-4}$. In Fig. 2(a), $-\log_{10}|e(t)|$ is shown for the three calculations, where $e(t)$ is the maximum error in position of the interface. There is a characteristic time, t_0, associated with each value of N. For $t \lesssim t_0$, the error stays within the round-off. After this time t_0, the error starts to increase quickly. This time corresponds to when the highest modes exceed the round-off. Soon thereafter the iteration ceases to converge, and the number of points needs to be increased to maintain spectral accuracy for the calculation and the convergence of the scheme. The time $t_0 \to t_c$ as N is increased. The shapes of the interface at $t=0$ and 0.54 from the calculation with $N=512$ are shown in Fig. 2(b). At $t=0.54$, the curvature at the tips is $|\kappa| \approx 253$, or 32 times its initial value. The zero-d_0 exact solution at $t=0.56$, right before t_c, is shown in a dashed curve. Three cusps are about to form at the tips of the interface.

Clearly the analytic frame provides a better discretiza-

tion for the evolution of the q-zero initial data than the Lagrangian one. The reason is straightforward. In the analytic frame we have

$$\frac{\partial z(p)}{\partial p}=ie^{ip}[1-u(t)e^{-3ip}].\qquad(19)$$

As $t \to t_c$, $u(t) \to 1$. Around the tip region, e^{-3ip} is close to 1, as a result, $\partial z(p)/\partial p \to 0$. That is, in the analytic frame more points are placed in the region with the largest curvature, while in the Lagrangian frame, the points are drawn away.

The story is quite different for the q-pole initial condition. In the analytic frame, the decay of the Fourier spectrum in p is governed by the distance of the poles to the unit circle. For $q=3$, $u_0=0.5$, and $v_0=0$, at $t=2.0$, $u \approx 0.9938$. That is, at $t=2.0$, the three poles of the derivative of the mapping function are very close to the unit circle; at least $N=8192$ points are needed so that the highest modes do not exceed the round-off.

Consider, on the other hand, the solution of Eqs. (8) and (9) in the Lagrangian frame using $N=256$ points and $\Delta t=10^{-4}$. Now, the solution agrees with the zero-d_0 exact solution to ten digits at $t=2.0$. The interfaces at times $t=0.0$, 0.5, 1.0, 1.5, and 2.0 are shown in Fig. 3. Note that the fjords, the places where the growth of the interface is greatly suppressed, have started to form.

To compare the two frames (analytic and Lagrangian), the Fourier amplitudes associated with each frame are shown at times 0.0, 0.5, 1.0, 1.5, and 2.0 in Fig. 4. Figure 4(a) shows the calculational results in the Lagrangian frame and Fig. 4(b) shows the zero-d_0 exact solutions in the analytic frame. In the Lagrangian frame, we have a full spectrum instead of just the zeroth and the negative modes in the analytic frame. Both sets of spectra show an overall exponential behavior which guarantees the convergence of the Fourier expansion. Starting with the same initial spectrum, the amplitudes associated with the La-
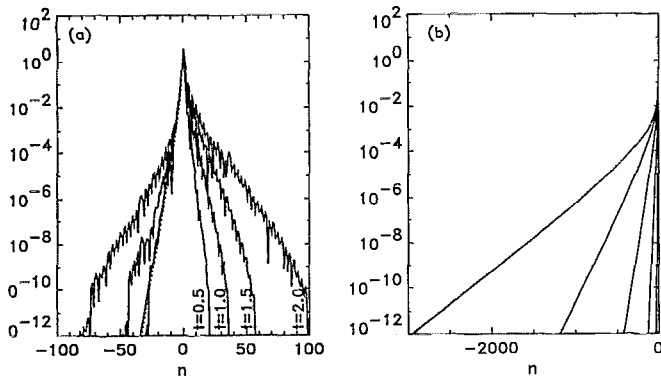
FIG. 4. Comparison of the Lagrangian frame and the analytic frame for the three-pole initial condition without surface tension as in Fig. 3. Absolute values of the Fourier modes versus frequency are shown. Note that the frequency scale is different for (a) and (b). (a) The Lagrangian frame. The dashed line corresponds to $t=0$. (b) The analytic frame. In this frame, only the zeroth mode and the negative modes exist. The lines from right to left correspond to the increasing times 0.0, 0.5, 1.0, 1.5, and 2.0.

grangian frame increase much more slowly in time. This allows us to use only 256 points to resolve the interface, even at time 2.0.

As was pointed out, the difference in the frames lies in how the initial discretization evolves on the interface. The distribution of 256 points (marked as "×") on one-third of the interface in the analytic frame at $t=2.0$ is shown in Fig. 5. Most of the points are away from the fjord region, leaving the fjord underresolved. This becomes obvious by examining

$$\frac{\partial z(p)}{\partial p} = ie^{ip} A(t) \frac{1-v(t)e^{-3ip}}{1-u(t)e^{-3ip}}. \tag{20}$$

At time 2.0, $v=0.6695...$, and $u=0.9938$, so $[1-u(t)] \ll [1-v(t)]$, which is also true for the later times.[16] At the bottom of the fjords, e^{-3ip} is close to 1 which makes $\partial z(p)/\partial p$ very large and as a result, the points are spread apart in
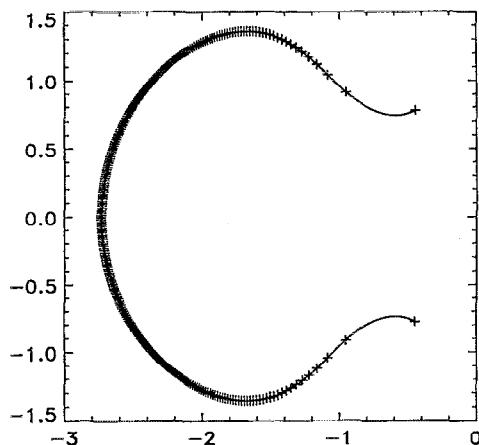

FIG. 5. The interface (one-third portion) without surface tension at time 2.0. The initial condition is the same as that in the previous two figures. "×" marks the distribution of 256 points in the analytic frame.

the fjord region. While in the Lagrangian frame, the points are advanced in time according to Eq. (9), whose second term in parentheses provides a pure tangential velocity which serves to move the points toward the fjord region.

VI. THE EVOLUTION UNDER SURFACE TENSION

Surface tension is the physically relevant regularization of interfacial motion in Hele–Shaw flow. In this section, we examine the expansion of the bubble under a small but finite surface tension. Numerical simulations of DKZ for the q-zero data show that the surface tension prevents the formation of a cusp by inducing a splitting of the singularities in the Riemann map. The outward cusp in the interface is replaced with an expanding bulb of fluid. However, for the q-pole initial condition, DKZ found it difficult to obtain numerically the long-time behavior, even though the underlying zero-d_0 exact solution exists for all time. Their numerical method is a pseudospectral technique, originally developed by Bensimon et al.,[15] for evolving the derivative of the Riemann map f. These difficulties may be related to the large gradients possible in the conformal map, as illustrated for this initial data by the zero-d_0 exact solutions given in the previous section. However, the short-time calculations of DKZ do indicate that under a small surface tension, the interfacial shape and the singularity structure of the Riemann map are similar to those of the zero-d_0 exact solution. We will concentrate on the q-pole initial data, and attempt to study the longer time dynamics. We are especially interested in the effect of a small and positive surface tension on the expanding bubble, as well as its sensitivity to noise.

A. The choice of the tangential velocity, $T(p)$

While the introduction of surface tension presumably regularizes the behavior of the interface, it also makes the resulting temporal evolution very stiff and necessitates the use of very small time steps. This stiffness problem is somewhat ameliorated by not allowing the computational points along the interface to become excessively clustered. Moreover, while the Lagrangian frame is better than the analytic one in this regard (and others), eventually the Lagrangian motion leaves the walls of the primary fjords overresolved relative to other portions of the interface. This increases the stiffness problem. For this reason, we introduce a frame which keeps points from becoming too clustered along the interface. Additionally, we find that this choice of frame leaves the interface better resolved than does the Lagrangian frame.

As an example, consider the pure tangential motion induced by

$$\frac{\partial z(p)}{\partial t} = \widetilde{T}(p) \frac{z_p(p)}{s_p(p)}, \tag{21}$$

where,

$$\widetilde{T}(p) = Cs_p(p)\mathscr{H}[s_q] \tag{22}$$

and $\mathscr{H}[\cdot]$ is the Hilbert transform[38] and C is a positive constant. Equation (21) implies that
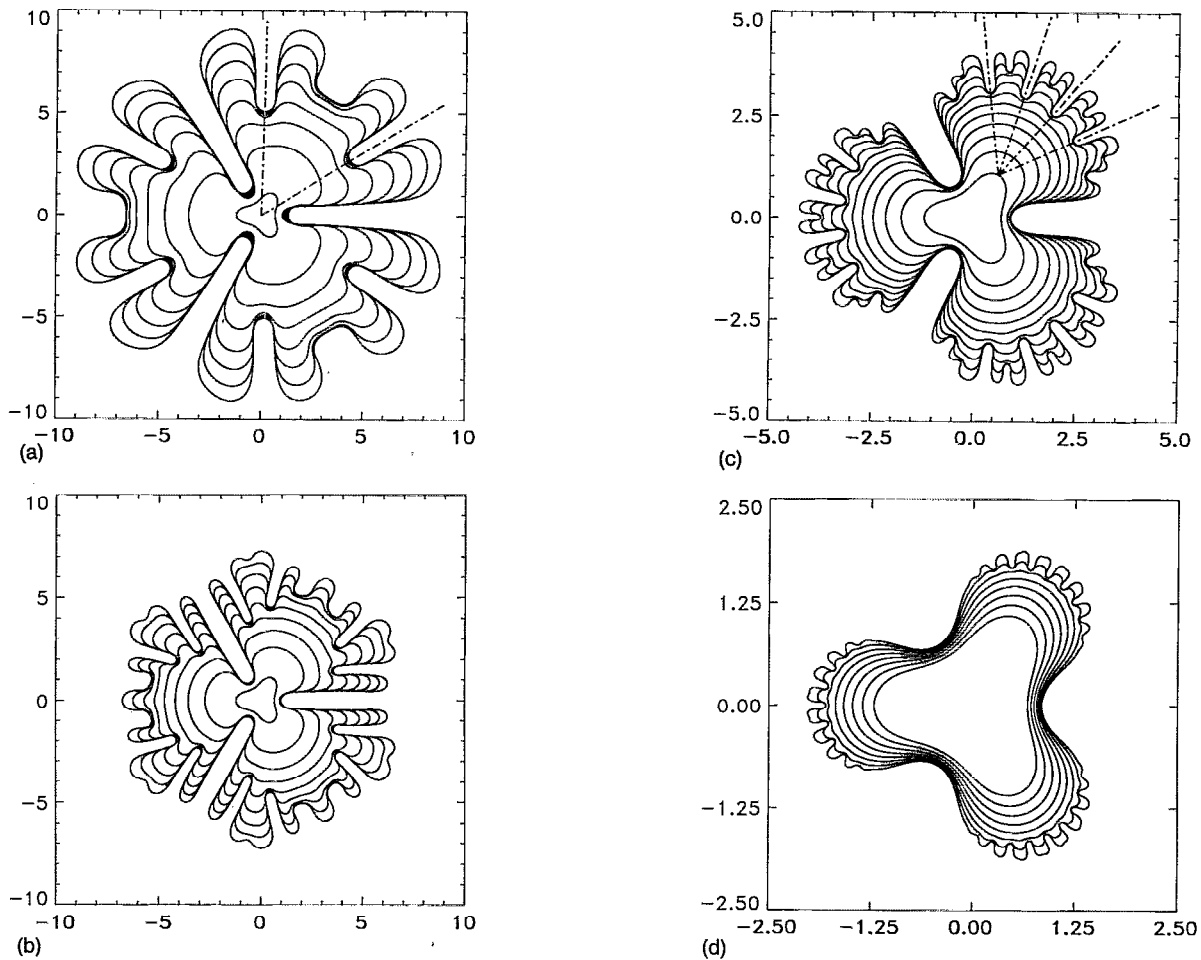
FIG. 6. Evolution of the interface starting with the three-pole initial condition (17) with $u_0=0.5$ for different surface tension parameters. (a) $d_0=4\times10^{-3}$, for times 0.0 to 28.0 with time increment 4.0. (b) $d_0=10^{-3}$, for times 0.0 to 16.0 with time increment 2.0. (c) $d_0=2.5\times10^{-4}$, for times 0.0 to 5.0 with time increment 0.5. [Note that it is on a scale half of (a) and (b).] (d) $d_0=6.25\times10^{-5}$, for times 0.0 to 0.7 with time increment 0.1. [Note that it is on a scale half of (c).]

$$\frac{\partial s_p(p)}{\partial t}=\widetilde{T}_p(p).\qquad(23)$$

Consider the case where the points are close to being evenly distributed in arclength, i.e., $s_p(p)=\bar{s}_p+\epsilon\delta(p)$, where, $\epsilon\ll1$ and $\bar{s}_p$ is the mean of s_p. Retaining terms up to first order in ϵ, Eq. (23) gives

$$\frac{\partial\delta(p)}{\partial t}=C\bar{s}_p\frac{\partial}{\partial p}\mathscr{H}[\delta].\qquad(24)$$

The Fourier transform diagonalizes Eq. (24), and for every Fourier mode δ_k with $k\neq0$ ($\bar{s}_p$ is fixed) we obtain

$$\frac{\partial\delta_k}{\partial t}=-(\epsilon C\bar{s}_p|k|)\delta_k.\qquad(25)$$

Thus, in this model problem with no normal motion, this choice of tangential velocity serves to drive the points toward a uniform distribution along the arclength. In the full problem, we partially exploit this property by defining

$$T(p)=\widetilde{T}(p)-\mathrm{Re}\left(Q^*[z(p)]\frac{z_p(p)}{s_p(p)}\right),\qquad(26)$$

and choose $C=0.1$. The second term above is the tangential fluid velocity, so (26) specifies that the only tangential motion that appears in Eq. (9) is that given by $\widetilde{T}$.

B. Results

1. General features

Figures 6(a)–6(d) show the evolution of the expanding bubble for the four (decreasing) values of the surface tension $d_0=4\times10^{-3}$, 10^{-3}, 2.5×10^{-4}, and 6.25×10^{-5}, respectively. Again, the initial interface is the q-pole initial condition with $q=3$ and $u_0=0.5$, shown as the innermost bubble. In each figure, the bubble position is shown at several times (see the figure captions for details). The calculation for a particular surface tension is stopped when it becomes necessary to increase N beyond 512. In general, the smaller the surface tension, the shorter the time over which the calculation could proceed. This results from the ramification of the interface due to the fingering structures (hereafter referred to as structures), whose time and space scales both decrease with d_0. For comparison, Fig. 7 shows the shapes at $t=25$, 15, 5, and 0.7 for $d_0=4\times10^{-3}$, 10^{-3}, 2.5×10^{-4}, and 6.25×10^{-5}, respectively, each superim-
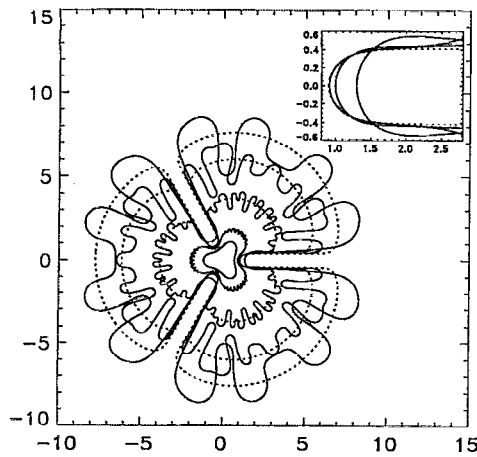
FIG. 7. Comparison of the bubble shapes at late times for different d_0's. The innermost bubble is the initial shape and the solid curves from the smallest to the largest correspond to the interface at time 0.7, 5, 15, 25, for $d_0=6.25\times10^{-5}$, 2.5×10^{-4}, 10^{-3}, and 4×10^{-3}, respectively. Each curve is superimposed with the zero-d_0 exact solution at the same time shown in a dashed curve. The insert shows the details of the bottoms of the primary channel region for the larger three d_0's.
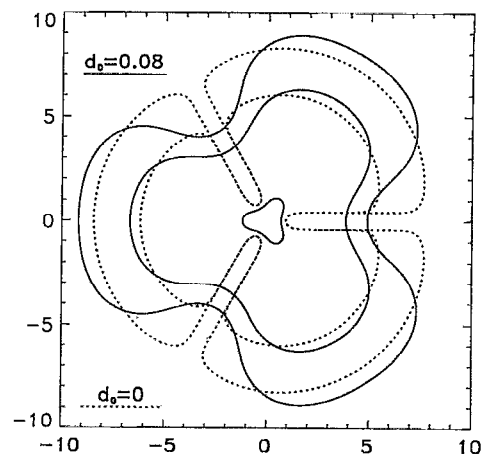

FIG. 8. The evolution of an interface with the same three-pole initial condition as that in Fig. 6, but with $d_0=0.08$. The innermost bubble shows the initial shape. The other two solid curves correspond to times 15 and 30, superimposed with the zero-d_0 exact solution at the same times.

posed with the exact zero-d_0 solution at that time (dashed curves). The innermost shape is again the initial bubble position. The insert shows the details of the bubbles at the bottom of the primary fjord for the larger three d_0's. These shapes are all calculated in 64-bit arithmetic.

For early times, the shape of the interface under surface tension varies little from that without surface tension. Except for the smallest value of d_0, for which the secondary structures form quickly, the three primary fjords form with or without surface tension; they are contained in the form of the initial data. Upon the formation of the primary fjords, the interface divides naturally into three regions: the channels which are formed by the sides of the primary fjords, the bottom of the fjord where the sides of the channel curve and meet, and the expanding fronts (the primary "petals") which are separated by the primary fjords.

When surface tension is present, the interface at the bottom of the primary fjords adjusts itself to even out the curvature and achieve a lower surface energy (proportional to the length of the interface). The larger the surface tension, the faster and larger is this adjustment. A similar behavior is also observed in the simulations of DeGregoria and Schwartz[26] in the channel geometry. The differences between "large" and "small" surface tensions can be striking. Let d_{c_1} be the surface tension parameter beyond which the linear growth of every mode is suppressed. For the initial condition used to generate Fig. 6, d_{c_1} is about 0.09. For d_0 larger than d_{c_1}, DKZ has observed that the fjords are suppressed and the interface tends toward circularity.[16] A circle is not likely to be the time-asymptotic state, since the effective surface tension decreases as the bubble expands, and any expanding near-circular bubble eventually becomes unstable. Figure 8 shows the interface at $t=0$, 15, and 30 in solid curves for $d_0=0.08$. The zero-d_0 exact solutions at the corresponding times are shown in dashed

curves. Here, d_0 is close to d_{c_1}, and the primary fjords have not developed even at very late times, causing substantial difference in the shape from that of the zero-d_0 exact solution. The d_0's in Fig. 6 are much smaller than d_{c_1}; the primary fjords develop as when d_0 is zero. The interface with the smallest d_0 in Fig. 6 is an exception, since 64-bit arithmetic was used in the simulation, the structures develop earlier than the primary fjords. The bottoms of the fjords are only moved slightly outwards. The channels of the primary fjords have all about the same width, determined by the initial data, up to a correction by the surface tension.

The behavior of the primary fjord regions is consistent with a uniform convergence to the underlying zero-d_0 exact solution. Conversely, the expanding front develops structures for every small but finite surface tension used, and any sense of uniform convergence to the almost circular front of the "limiting" solution is not apparent (see Fig. 7).

The structures appear first by ripples developing somewhere along on the front. For the two larger d_0's [Figs. 6(a) and 6(b)] these ripples occur on the sides of the primary petals, adjacent to the primary fjords, while for the smaller d_0's [Figs. 6(c) and 6(d)] the ripples occur across the center of a primary petal. One might refer to the first as side branching and the second as tip splitting. This behavior is partially consistent with the experimental results of Tabeling et al. on the stability of viscous fingers in a channel.[21] They found that at lower velocities (higher surface tension), the instability first observed occurred (asymmetrically) at the sides of the finger, while at higher velocities (lower surface tension) the first instability was tip splitting. The stability of the petal center at higher surface tension may be related to a stabilizing mechanism through which perturbations are convected toward the channels away from the petal center, similar to the stability of a propagating flame front[39] and the stability of a curved

front such as a Saffman–Taylor finger or dendritic crystal.[40]

From the ripples there develop both straight, growing fingers, like those at the sides of the primary fjords in Fig. 6(b), and more typical expanding fingers, which we follow Ben Amar[6] in calling "petals." The straight Saffman–Taylor fingers are well studied in the channel geometry.[3] The expanding petals seem to be unique to the sector and circular geometries. The sector geometry refers to flow between two diverging slip walls, with the mass source of inviscid fluid at their intersection. Interest in this geometry arose from it being intermediary between channel and circular geometries.[4–8] Petals in the sector geometry are the analog to Saffman–Taylor fingers in the channel, with the sector and petal angles playing the respective roles of channel and finger widths. Similarity solutions have been found and angle selection by surface tension has been studied. It was found that the selected petal solution ceases to exist when the petal becomes sufficiently large. Thomé et al. studied experimentally petal growth in the sector geometry and found an eventual tip-splitting instability that allows the petal to bifurcate and restabilize temporarily at a smaller effective sector angle.[4] In the circular geometry they were able to fit petal profiles to those obtained in a sector with a correspondingly chosen angle. As in the sector geometry, these observed petals eventually become unstable to tip splitting.

A similar situation is observed here, where expanding petals are observed for all small but nonzero surface tensions. The tip splitting is most apparent at the smallest d_0, occurring atop every secondary petal. In the circular geometry, the experimenters were able to extrapolate the effective sector sides of an observed petal and found their intersection to be the mass source at the center. Here this property is only present for the largest d_0 [note the sector lines drawn in Fig. 6(a) as the dot-dash lines]. For the $d_0 = 2.5 \times 10^{-4}$, the interior sectors for the expanding petals meet not at the origin, but rather near the protruding tip of the initial bubble [note the sector lines drawn in Fig. 6(c) as the dot-dash lines]. In this case, the primary fjord is dominant and apparently shields the true mass source, and creates in its stead an effective one.

For an interface with surface tension, the result of linear analysis on an expanding circle provides a maximum growth mode with a characteristic length scale. When the length of the interface is of the order of this length scale, ripples develop on the interface, as has been observed experimentally in channel, sector, and circular geometries.[41,21,4,11] For d_0 used in Fig. 6, the dependence of this length scale on d_0 is roughly $d_0^{1/2}$. When d_0 is decreased by a factor of 4, the size of the secondary fjords which separate the secondary petals is decreased by a factor of 2.

The shape of the interface at late stages of the fingering process resembles those obtained via diffusion limited aggregation (DLA)[42] (for DLA, see for example, Ref. 43). Experiments in porous media also show similar shapes.[44] In log–log scale for $d_0 = 0$ and the larger three d_0's in Fig. 6, Fig. 9 shows the bubble area $S(t)$ vs $D(t)$, the "radius
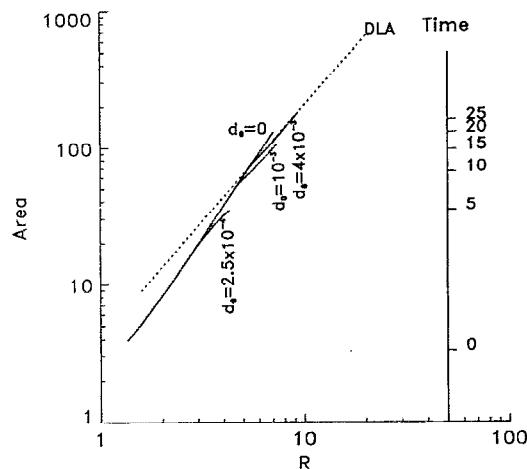

FIG. 9. Bubble area $S(t)$ versus radius of gyration $D(t)$ in log–log scale. The dashed line has a slope of 1.7, as calculated for DLA. The right vertical axis gives the time scale.

of gyration." Here, $D(t)$ is defined as the maximum distance of a point on the interface from the injection point. The radius of gyration has been used as a measurement of complexity, as the slope of $\log D$ vs $\log S$ gives roughly d, where d is the dimension of the bubble of fluid 1. For example, the slope is two for a circular bubble. The slope for zero-d_0 solution is 2.1, but this is because the bubble is not yet large enough to ignore the area taken by the channels. Initially the positive d_0 curves follow the zero-d_0 one. When the ripples appear, the slope starts to decrease. The dashed line has a slope of 1.7, which is the corresponding slope from DLA.[43]

2. Effect of noise and surface tension

The results of the previous section leave us with an apparent paradox. As the zero-d_0 exact solution for the q-pole initial condition does not develop unbounded curvature, perhaps small d_0 acts as a regular perturbation of the system. Indeed, the short time numerical results of DKZ showed convergence of the computed solution to the zero-d_0 exact solution as $d_0 \to 0$. However, that limit also takes us to an ill-posed system. Our long-time solutions for small and positive d_0 differ from that for zero-d_0 fundamentally in that secondary structures develop. Further, Figs. 6 and 9 show that the structures develop earlier for smaller d_0, which suggests that the surface tension might be a singular perturbation when long time behavior is concerned. To study this question, we will first concentrate on the onset of rippling, and its dependence on noise and surface tension.

We start by identifying features in curvature that result in rippling in order to define an onset time, t_c^n, which marks a significant departure from the zero-d_0 exact solution. Figures 10(a)–10(d) show curvature versus arclength at the times 1.0, 1.5, 2.0, and 2.5, respectively, where the arclength is measured from the bottom of a fjord to the center of an adjacent front. The solid curves correspond to results for $d_0 = 2.5 \times 10^{-4}$ calculated in 64-bit arithmetic.
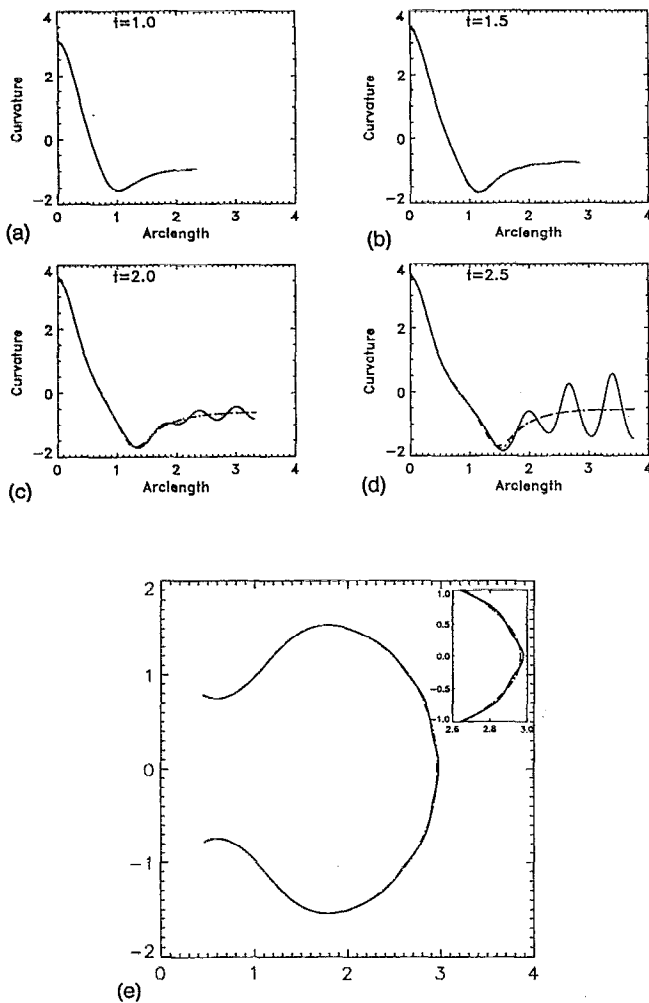
(a), (b), (c), (d) curvature-versus-arclength plots at $t=1.0$, 1.5, 2.0, 2.5; (e) interface plot.

FIG. 10. Comparison of the zero-d_0 exact solutions (long-dashed curves) and the simulational results for $d_0 = 2.5 \times 10^{-4}$ with 64-bit arithmetic (solid curves) and 128-bit arithmetic (short-dashed curves). (a)–(d) Curvature versus arclength, measured from the bottom of a fjord to the center of a neighboring front, for the respective times 1.0, 1.5, 2.0, and 2.5. (e) The interface (one-third portion) at time 2.5 for the three cases. The insert shows the details of the front of the interface.

The long-dashed curves correspond to the zero-d_0 solution. At early times, little difference is observed between them, especially at the front region [Fig. 10(a)]. Soon, however, oscillations develop in the $d_0 = 2.5 \times 10^{-4}$ solution [Fig. 10(b)], the amplitudes of which increase in time [Fig. 10(c)]. When the sign of curvature oscillates along the front [Fig. 10(d)], the ripples are apparent as shown in Fig. 10(e). These oscillations in curvature that precede the apparent ripples are observed for all positive d_0 considered here with $d_0 < 0.1 d_{c_1}$. We identify the onset of the oscillations with the onset of rippling and define t_c^n to be the time when a new local extremum in curvature just develops along the front. For example, $t_c^n \approx 1.2$ for $d_0 = 2.5 \times 10^{-4}$.

In the case of the Saffman–Taylor finger solutions in a channel geometry, although there is one finger that is linearly stable when surface tension is present,[3] both simulation and experimental results show that it can undergo instability when it is perturbed by a disturbance with a finite amplitude.[26,27,41,21] DeGregoria and Schwartz's nu-

merical studies[26,27] and Bensimon's analysis[45] show that noise plays an important part in the stability properties of the interface. In particular, a heuristic analysis of Bensimon suggests that the minimum amplitude of noise needed to drive the finger solution unstable decreases exponentially with d_0. Numerical simulations reveal that the finger that undergoes instability bifurcates (tip splitting).[26,27,46] A natural question arises on the nature of the structures seen here: Are they only amplification of noise—say the round-off in the arithmetic, or are they intrinsic to the initial condition (17) under evolution equations (8) and (9)?

We employ a simple linear model to study the evolution of noise. Because of its expansion, the front of the bubble is the most unstable region of the interface. Accordingly, we consider the linear evolution of noise-seeded perturbations by (11):

$$\dot{a}_n(t) = \sigma_{3n}(t) a_n(t), \qquad (27)$$

where $R(t)$ is chosen to be that at the front center for the zero-d_0 solution [also setting $dS/dt = 2\pi R(t) dR(t)/dt$]. The center has the greatest radius of curvature along the front, and the zero-d_0 behavior there describes well the behavior for small and positive surface tension before the onset time t_c^n. To account for the symmetry factor $q = 3$, we consider only $k = 3n$ in (11).

The initial values for a_n should be chosen to reflect the initial "noise" in that mode. However, it is unclear how this should be done. Here, the noise is simply chosen to be a constant background amplitude by

$$a_n(t) = c\epsilon. \qquad (28)$$

For example, $c\epsilon$ might be chosen as the filtering level of the calculation (10^{-12} for 64-bit arithmetic). However, we find that the time scale of growth in this model describes best that in the full calculation if we multiply the filter level (now ϵ) by a factor 10^4 (now c). One reason for this might be that the real noise on the important modes in the calculations is multiplied by a number of derivatives [for example, the three derivatives to form γ in Eq. (8)]. And obviously, the effect of nonlinearity is not being accounted for. At any rate, the model is only intended to provide a rough description of the growth of noise, which it does.

Figure 11 shows a_n vs n for $d_0 = 2.5 \times 10^{-4}$ from $t = 0$ to 1.4. Only a band of the lower modes is amplified, and there is a mode of maximum amplitude (marked by "$\times$"). Since the effective surface tension decreases as the radius of curvature increases, this mode shifts to higher values of n. The linear onset time, t_c^L, is defined to be the time at which an amplitude reaches 1% of $R(t)$. These features are results of the growth rate (11), not the results of particular size of the initial conditions. Figure 12 shows the growth of the lowest 40 modes in the Riemann map from the full calculation, in semi-log scale, at the times 0, 1.0, 2.0, and 3.0. Although nearly all modes grow in time unlike in the linear results, there is a band of modes in which some modes grow faster than their neighbors. The one with the highest amplitude is about the seventh, agreeing with the corresponding one in linear results shown in Fig. 11. This
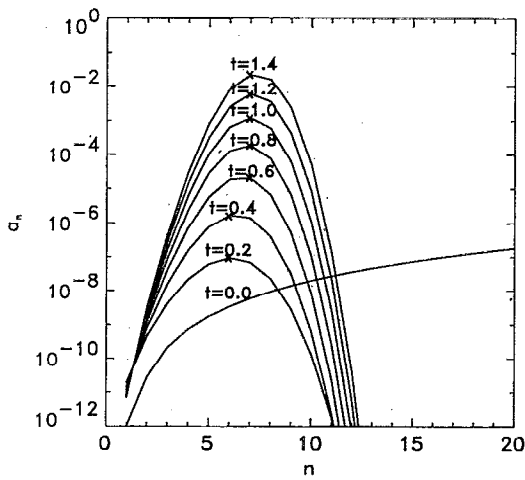
FIG. 11. The results for the linear model (27). a_n, the amplitude of the mode n added to an expanding circle, versus n is shown in semilog scale for $t=0.0$ to 1.4. The mode with the maximum amplitude for $t>0$ is marked by "$\times$".

mode number is also consistent with the number of ripples developed along the front. We obtain that, for $d_0 = 2.5 \times 10^{-4}$, t_c^L is about 1.28, close to t_c^n.

Figure 13 shows the dependence of t_c^L (solid curve) and t_c^n (marked by "$+$") on d_0. There is a change in behavior in t_c^n at $d_0 \equiv d_{c_2} \approx 5 \times 10^{-4}$. For $d_0 < d_{c_2}$, t_c^L and t_c^n roughly agree with each other, while they differ drastically for $d_0 > d_{c_2}$. Another important feature of the dependence of t_c^n on d_0 is that t_c^n increases with increasing d_0 for $d_0 \leqslant d_{c_2}$ while it decreases for $d_0 > d_{c_2}$. Again we want to point out that although changing the factor on ϵ in (28) will change the exact agreement in the numbers of t_c^n and t_c^L for $d_0 < d_{c_2}$, the trend of their dependence on d_0 will not be changed. We also note here that t_c^n is not the same time as the slope deviation from the zero-d_0 result in Fig. 9. Due to its nonlocal nature, that deviation is a relatively insensitive
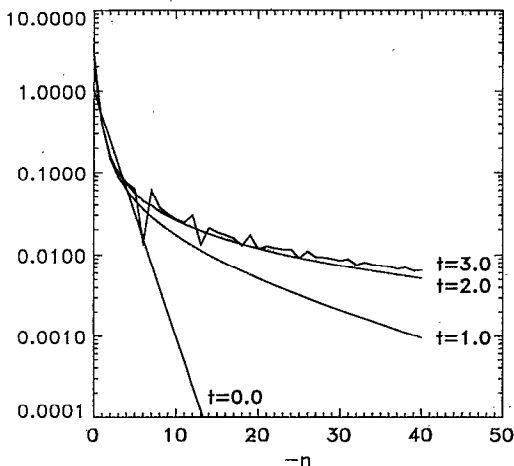

FIG. 12. Absolute values of the lowest 40 Fourier modes of the Riemann mapping function versus frequency $-n$ in semilog scale at times 0.0, 1.0, 2.0, and 3.0 for results with $d_0 = 2.5 \times 10^{-4}$ calculated in 64-bit arithmetic.
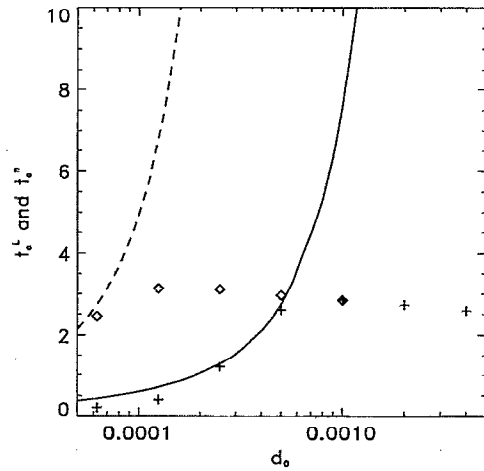

FIG. 13. Comparison of the dependence of t_c^L and t_c^n upon d_0. t_c^L is determined through the linear model (27); t_c^n is determined through the full calculation. The solid and the dashed curves are t_c^L with $\epsilon = 10^{-12}$ and 10^{-26}, respectively. The points marked by "$+$" and "$\diamond$" are t_c^n as calculated from 64- and 128-bit results, respectively.

measure of the onset since it is not observed until the secondary fjords are well formed. We will demonstrate the differing effects of noise, for d_0 in the different regimes, by showing differing response to noise of varying amplitude.

We first increase the size of noise by adding a noise term of size ϵ to (17):

$$z(p) = e^{ip} \sum_{n=-\infty}^{0} \frac{u_0^{-n}}{1+qn} e^{iqnp} + \epsilon e^{ip} \sum_{n=1}^{M} e^{-iqnp}. \quad (29)$$

The previous calculations in 64-bit arithmetic are equivalent to having ϵ of order 10^{-12}. Here we choose $M = 50$ and $\epsilon = 10^{-10}$ for comparison. Figure 14(a) shows the shapes for $d_0 = 2.5 \times 10^{-4}$ at the times 0, 0.5, 1.0, 1.5, and 2.0. Figure 14(b) shows the shapes for $d_0 = 10^{-3}$ at the times 0, 1, 2, 3, 4, and 5. The long- and short-dashed curves correspond, respectively, to results from initial conditions (29) with $\epsilon = 10^{-10}$ and (17) [effectively $\epsilon = 10^{-12}$ in (29)]. Only one-third of the interface is shown. In Fig. 14(b), the zero-d_0 exact solution at $t = 5.0$ is also shown in a solid curve. For $d_0 = 2.5 \times 10^{-4}$, the interface with larger initial "noise" develops ripples earlier, with t_c^n about 0.8. This onset time agrees well with the linear onset time, (t_c^L), if we set $\epsilon = 10^{-10}$ in (28). Similarly, we can obtain a t_c^L for each corresponding t_c^n by choosing ϵ in (28) to be the same value as that in (29). Figure 15 shows the dependence of t_c^L (marked as "Δ") and t_c^n (marked as "$+$") upon ϵ, for $d_0 = 2.5 \times 10^{-4}$. The times t_c^L and t_c^n agree roughly with one another for $\epsilon \leqslant 10^{-10}$, while they disagree for $\epsilon > 10^{-8}$. The disagreement could be due to the following: the larger values of ϵ are close to or larger than the initial values of the fastest growing modes, and as a result, the dynamics is significantly altered and not captured in the linear model. At any rate the results for $d_0 = 2.5 \times 10^{-4}$ are consistent with the assumption that amplified noise is responsible for generating the structures. But for $d_0 = 10^{-3}$, the interface
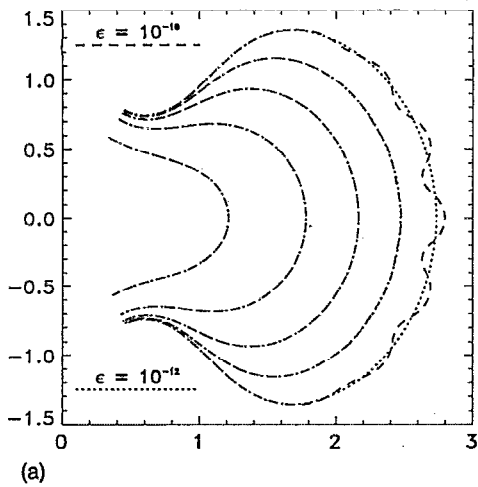
(a)
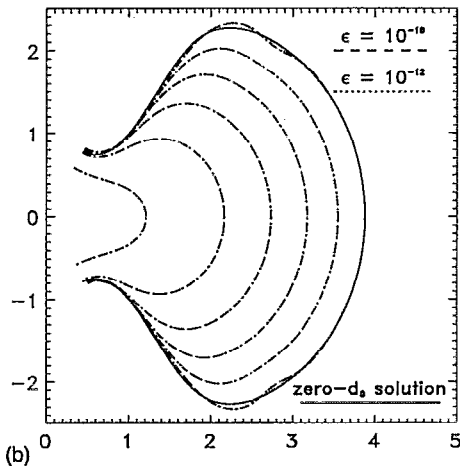
(b)

FIG. 14. Comparison of the interface shapes (one-third portion is shown) calculated in 64-bit arithmetic with different sizes of initial "noise." The long-dashed curves are from initial condition (29) with $\epsilon = 10^{-10}$, and the short-dashed curves with $\epsilon = 10^{-12}$. (a) $d_0 = 2.5 \times 10^{-4}$ at the times 0, 0.5, 1.0, 1.5, and 2.0. (b) $d_0 = 10^{-3}$ at the times 0, 1, 2, 3, 4, and 5. The solid curve is the zero-d_0 exact solution at $t = 5.0$.

shows an insensitivity to noise: t_c^n does not change with the size of ϵ, and neither does the evolution of the interface shapes.

We then decrease the size of noise by carrying out the calculations in 128-bit arithmetic on a Cray Y-MP. The results for $d_0 = 2.5 \times 10^{-4}$ are shown in Figs. 10(a)–10(e) (short-dashed), in comparison with the 64-bit arithmetic results (long-dashed curves) and the zero-d_0 exact solution (solid curves). For $d_0 = 10^{-3}$, Fig. 16 shows curvature versus arclength, measured from the bottom of a fjord to the center of a neighboring front, at $t = 3.5$ from 128- and 64-bit arithmetic results in long- and short-dashed curves, respectively. The solid curve corresponds to the zero-d_0 exact solution. Again, we see the contrast in the behavior with different d_0. For $d_0 = 2.5 \times 10^{-4}$, the results from 128-bit arithmetic differ little from the zero-d_0 exact solution even after t_c^n associated with 64-bit calculations. For $d_0 = 10^{-3}$ the 64- and 128-bit arithmetic results differ little from each other, showing an insensitivity to the noise level, and they both differ from the zero-d_0 exact solution at later times by developing oscillations in curvature or ripples on the interface.
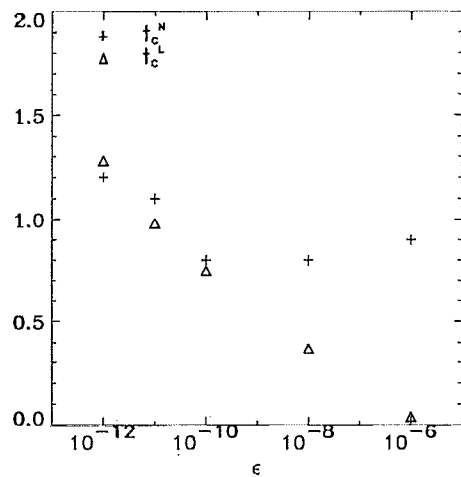

FIG. 15. Comparison of the dependence of t_c^L (marked as "Δ") and t_c^n (marked as "$+$") upon ϵ. The initial condition is (29), and the calculation is performed in 64-bit arithmetic.

The different regimes of d_0 shown in Fig. 13 can be explained by the different roles played by noise. For $d_0 \ll d_{c_2}$, the round-off in 64-bit arithmetic is amplified to eventually give rise to the structures [see Figs. 6(c) and 6(d)]. Some general features of the amplification process are captured in the linear model (27), in particular the model gives a good estimate of the time scale of the process under the full equations. For $d_0 > d_{c_2}$, the structures [Figs. 6(a) and 6(b)] are intrinsic and insensitive to noise.

A consistent picture of the effect of noise and surface tension on the structures results from the above tests. In Fourier space, the structures correspond to the band of modes which contains those modes that grow faster than their neighbors (Fig. 12), the cutoff to which is denoted as n_c. The n_c can be roughly estimated from the cutoff to the only band of modes that is amplified in the linear model
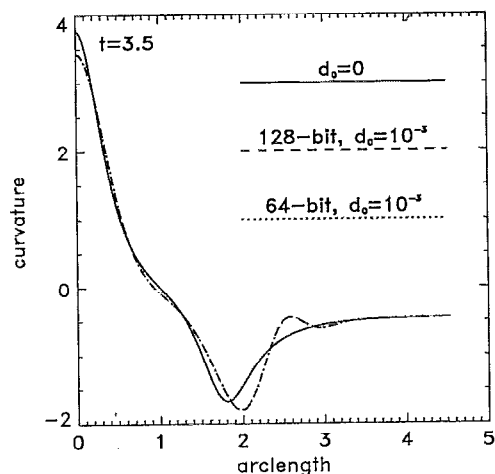

FIG. 16. Comparison at $t = 3.5$ of the zero-d_0 exact solution and the 64- and 128-bit calculations for $d_0 = 10^{-3}$. The curves are curvature versus arclength measured from the bottom of a fjord to the center of an adjacent front.

(27) (Fig. 11), although the linear model gives a under-estimation because nonlinear coupling between the modes is not considered. Initially, every mode is comprised of a "pure" part from (17): $|f_n| = u_0^n/(qn-1)$, which is a decreasing function in n, and a noise part. Both parts are amplified under Eqs. (8) and (9). When some of them have grown to be larger than their neighbors, structures characterized by them become apparent. If initially these modes, especially $|f_{n_c}| = u_0^{n_c}/(qn_c - 1)$, are comparable to noise, some significant part of the amplified modes which determine the structures comes from amplified noise. If initially these modes are much larger than noise, the later values of these modes come mostly from the "pure" initial condition and thus are insensitive to noise. Since smaller d_0 leads to larger n_c [see (11)] and in turn leads to smaller $|f_{n_c}|$, the effect of noise depends on the size of d_0. For example, when $u_0 = 0.5$ and $q = 3$, for $d_0 = 2.5 \times 10^{-4}$, $n_c \approx 35$ and $|f_{n_c}| \approx 10^{-13}$, while $|f_{n_c}| \approx 10^{-7}$ for $d_0 = 10^{-3}$. In 64-bit arithmetic, the different comparative size of $|f_{n_c}|$ to the round-off, leads to different response to noise reflected in the simulation results.

We conclude this section by going back to the question raised at the beginning on the effect of the surface tension. Since we are interested in the difference of the solution with or without surface tension, we will again concentrate on the quantity t_c^n. In order to obtain the "true" behavior, which is not dominated by the effect of noise, we need to identify a "true" t_c^n associated with d_0. From the previous understanding of the effect of noise, we can assume that this "true" t_c^n can be obtained by using 64-bit arithmetic for $d_0 > d_{c_2}$ while using more precise arithmetic for $d_0 < d_{c_2}$. Figure 13 shows t_c^n obtained from 64- and 128-bit arithmetic marked by "$+$" and "$\Diamond$," respectively, for several d_0's. Also shown in dashed curve is t_c^L associated with 128-bit arithmetic by setting $\epsilon = 10^{-26}$ in (28). The fact that t_c^n for $d_0 = 6.25 \times 10^{-5}$ from 128-bit arithmetic (the leftmost "$\Diamond$") agrees with the above associated t_c^L indicates that for this very small d_0, even 128-bit arithmetic is not precise enough to avoid the effect of noise. Here $d_0 = 5 \times 10^{-4}$ seems to be a transition value: even though t_c^n agrees with t_c^L in 64-bit arithmetic, t_c^n from 64- and 128-bit arithmetic results are close to each other too. This is probably because the size of the cutoff to the modes that determine the structures is close to the round-off in 64-bit arithmetic. We also note here that there is a correlation between the initial rippling process and the agreement or disagreement between t_c^n and the associated t_c^L. For those d_0 whose t_c^n agrees with the associated t_c^L, as has been observed for $d_0 = 2.5 \times 10^{-4}$, the effect of noise is strong, and we observe that the initial ripples occur across the front of the interface (tip splitting). For an interface insensitive to noise, the initial rippling is side branching. Discarding those values of t_c^n believed to be in the noise-dominant regime, we observe a monotonic increase of t_c^n with decreasing d_0.

This is a strong indication that a small surface tension is a regular perturbation to the Eqs. (8) and (9) under the pole initial condition of the form (17). There are qualifications. A referee has pointed out that an asymptotic anal-

ysis of Tanveer[20] predicts the formation in the unphysical domain of "daughter singularities" from initial zeros in g. These singularities begin with zero amplitude, and for short times increase in amplitude with some positive power of $d_0 t$. Leaving aside questions of the structural stability of these objects, or whether Tanveer's analysis is applicable here, there is the possibility that the Fourier filtering used in the numerical method could "erase" such newly born singularities. For particular cases, we have studied carefully the effect of both the filter level and the time step. For example, for $d_0 = 10^{-3}$, we decreased both the filter level (from 10^{-12} to 10^{-26}), and the time step (from 10^{-3} to 10^{-4}), and saw no change in the behavior. The decrease in filter level and time step should allow more dynamical range in the spectrum, and more accuracy in the time integration, respectively. Nonetheless, it may be that such new structures would manifest themselves only on longer time scales than we have investigated here, or that there is not yet sufficient dynamical range to observe them.

VII. CONCLUSIONS

We have implemented numerically a boundary integral formulation of the Hele–Shaw problem. This method is spectrally accurate in space and fourth order in time. In order to maintain resolution of the bubble interface under surface tension, and to minimize the associated stiffness of the system, a tangential velocity was added along the interface to prevent computational points from clustering excessively. For the q-pole initial condition, we have been able to continue the simulation long enough to observe the formation of new structures on the interface that are produced by the surface tension. By varying both the precision of the calculation and explicitly adding "noise" to the initial data, we were able to distinguish between structures arising through the intrinsic action of surface tension, and structures arising through the growth of numerical noise at scales allowed by the surface tension (under the qualification stated above). Side branching seems to be the intrinsic response of the system to surface tension, while tip splitting is associated with the growth of noise.

We found also that for this particular initial condition (i.e., the initial analytic structure of g contains pure poles and no zeros), the time scale for the occurrence of such side branching increases with decreasing surface tension. In particular it is consistent with a logarithmic behavior for this time scale (as seen in Fig. 13) that has now been predicted by Tanveer for this specific case.[47] Lacey et al.[17] have attempted to model the effect of surface tension for cases when cusps form in the limiting zero surface tension solution. Implicit in their treatment is the assumption that surface tension is important only in the neighborhood of large curvature. In this sense, as the limiting solution has bounded curvature, our results for this initial data agree with this assumption. However, Tanveer[20,47] has also conjectured that there are initial conditions for which the zero surface tension solution has bounded curvature (and is smooth), yet manifests structure in the presence of surface tension whose onset time does not go to infinity with de-

creasing surface tension. In collaboration with Tanveer, we are currently investigating such a possibility.

ACKNOWLEDGMENTS

APPENDIX: THE ANALYTIC FRAME

The complex velocity of the interface can be separated into a normal and a tangential component,

$$\frac{\partial z(p)}{\partial t} = -iz_p(p)\left(\frac{V_n(p)}{|z_p(p)|} + i\frac{V_t(p)}{|z_p(p)|}\right). \tag{A1}$$

Here $V_n(p)$ and $V_t(p)$ are real and periodic functions with periodicity 2π, which are given by projecting the velocity onto the normal and tangential directions, respectively,

$$V_n(p) = \text{Im}\left(\frac{\partial z^*(p)}{\partial t}\frac{z_p(p)}{|z_p(p)|}\right)$$

$$= \text{Im}\left[\frac{z_p(p)}{|z_p(p)|}\left(\frac{dS/dt}{2\pi}\frac{1}{z(p)}\right.\right.$$

$$\left.\left. + \frac{1}{2\pi i}P\oint_{\partial\Omega}\frac{\gamma(q)}{z(p)-z(q)}dq\right)\right],$$

$$V_t(p) = \text{Re}\left(\frac{\partial z^*(p)}{\partial t}\frac{z_p(p)}{|z_p(p)|}\right)$$

$$= T(p) + \frac{1}{2}\frac{\gamma(p)}{|z_p(p)|}$$

$$+ \text{Re}\left(\frac{z_p(p)}{|z_p(p)|}\frac{1}{2\pi i}P\oint_{\partial\Omega}\frac{\gamma(q)}{z(p)-z(q)}dq\right). \tag{A2}$$

To retain the points in the analytic frame, the function $V_t(p)$ is chosen to make the velocity (A1) an analytic function for p not only on the real axis, but also extended to the upper half of the complex-p plane,

$$V_t(p) = iV_n(p) - i|z_p(p)|\hat{A}\left(\frac{V_n(p)}{|z_p(p)|}\right), \tag{A3}$$

where $\hat{A}$ is an analytic continuation operator which is defined as follows.[15] For a function $F(p) = \Sigma_{n=-\infty}^{\infty}a_n e^{inp}$,

$$\hat{A}\{F(p)\} = a_0 + 2\sum_{n<-1}a_n e^{inp}. \tag{A4}$$

Finally, the expression for $T(p)$ is obtained by putting Eqs. (A2) into Eq. (A3),

$$T(p) = iV_n(p) - i|z_p(p)|\hat{A}\left(\frac{V_n(p)}{|z_p(p)|}\right) - \frac{1}{2}\frac{\gamma(p)}{|z_p(p)|}$$

$$- \text{Re}\left(\frac{z_p(p)}{|z_p(p)|}\frac{1}{2\pi i}P\oint_{\partial\Omega}\frac{\gamma(q)}{z(p)-z(q)}dq\right). \tag{A5}$$

[1] P. A. Zhuralev, Zap. Leningr. Com. Inst. 33, 54 (1956) (in Russian). For early Soviet work in the porous media context see also P. Ya. Pulubarinova-Kochina, Theory of Ground Water Movement (Princeton University Press, Princeton, 1962).

[2] P. G. Saffman and G. I. Taylor, "The penetration of a fluid into a porous medium or Hele–Shaw cell containing a more viscous liquid," Proc. R. Soc. London Ser. A 245, 312 (1958).

[3] For a review of the subject and some related topics, see Dynamics of Curved Fronts, edited by P. Pelcé (Academic, San Diego, 1988), and references therein.

[4] H. Thomé, M. Rabaud, V. Hakim, and Y. Couder, "The Saffman–Taylor instability from the linear to the circular geometry," Phys. Fluids A 1, 224 (1989).

[5] Y. Tu, "Saffman–Taylor problem in sector geometry: Solution and selection," Phys. Rev. A 44, 1203 (1991).

[6] M. Ben Amar, "Exact self-similar shapes in viscous fingering," Phys. Rev. A 43, 5724 (1991).

[7] M. Ben Amar, V. Hakim, M. Mashaal, and Y. Couder, "Self-dilating viscous fingers in wedge-shaped Hele–Shaw cells," Phys. Fluids A 3, 2039 (1991).

[8] R. Combescot and M. Ben Amar, "Selection of Saffman–Taylor fingers in the sector geometry," Phys. Rev. Lett. 67, 453 (1991).

[9] L. Paterson, "Radial fingering in a Hele–Shaw cell," J. Fluid Mech. 113, 513 (1981).

[10] L. Paterson, "Fingering with miscible fluids in a Hele–Shaw cell," Phys. Fluids 28, 26 (1985).

[11] S. N. Rauseo, P. D. Barnes, Jr., and J. V. Maher, "Development of radial fingering patterns," Phys. Rev. A 35, 1245 (1987).

[12] B. Shraiman and D. Bensimon, "Singularities in nonlocal interface dynamics," Phys. Rev. A 30, 2840 (1984).

[13] S. D. Howison, "Fingering in Hele–Shaw cell," J. Fluid Mech. 167, 439 (1986).

[14] S. Sarkar and M. Jensen, "Interface dynamics and directional solidification: A lattice simulation with biased random walkers," Phys. Rev. A 35, 1877 (1987).

[15] D. Bensimon, L. P. Kadanoff, S. Liang, B. I. Shrainman, and C. Tang, "Complex analytic viscous flows in two dimensions," Rev. Mod. Phys. 58, 977 (1986).

[16] W.-S. Dai, L. P. Kadanoff, and S.-M. Zhou, "Interface dynamics and the motion of complex singularities," Phys. Rev. A 43, 6672 (1991).

[17] A. A. Lacey, S. D. Howison, J. R. Ockendon, and P. Wilmott, "Irregular morphologies in unstable Hele–Shaw free-boundary problems," Q. J. Mech. Appl. Math. 43, 387 (1990).

[18] P. Constantin and L. Kadanoff, "Singularities in complex interface," Philos. Trans. R. Soc. London Ser. A 33, 379 (1990).

[19] P. Constantin and L. Kadanoff, "Dynamics of a complex interface," Physica D 47, 450 (1991).

[20] S. Tanveer, "Evolution of Hele–Shaw interface for small surface tension," submitted to Proc. R. Soc. London Ser. A 343, 1 (1993).

[21] P. Tabeling, G. Zocchi, and A. Libchaber, "An experiment study of the Saffman–Taylor instability," J. Fluid Mech. 177, 67 (1987).

[22]R. Krasny, "Desingularization of periodic vortex sheet roll-up," J. Comput. Phys. **65**, 292 (1986).

[23]G. R. Baker and M. J. Shelley, "On the connection between thin vortex layers and vortex sheets," J. Fluid Mech. **215**, 161 (1990).

[24]G. R. Baker, D. I. Meiron, and S. A. Orszag, "Generalized vortex methods for free-surface flow problems," J. Fluid Mech. **123**, 477 (1982).

[25]G. Tryggvason and H. Aref, "Numerical experiments on Hele–Shaw flow with a sharp interface," J. Fluid Mech. **136**, 1 (1983).

[26]A. J. DeGregoria and L. W. Schwartz, "Finger breakup in Hele–Shaw cells," Phys. Fluids A **28**, 2313 (1985).

[27]A. J. DeGregoria and L. W. Schwartz, "A boundary-integral method for two-phase displacement in Hele–Shaw cells," J. Fluid Mech. **164**, 383 (1986).

[28]D. Kellogg, *Foundations of Potential Theory* (Dover, New York, 1929).

[29]W. W. Mullins and R. F. Sekerka, "Morphological stability of a particle growing by diffusion or heat flow," J. Appl. Phy. **34**, 323 (1963).

[30]A. Sidi and M. Israeli, "Quadrature methods for periodic singular and weakly singular Fredholm integral equations," J. Sci. Comput. **3**, 201 (1988).

[31]M. Shelley, "A study of singularity formation in vortex sheet motion by a spectrally accurate vortex method," J. Fluid Mech. **244**, 493 (1992).

[32]R. Krasny, "A study of singularity formation in a vortex sheet by the point vortex approximation," J. Fluid Mech. **167**, 65 (1986).

[33]R. Caflisch, T. Hou, and J. Lowengrub, "Convergence of numerical methods for ill-posed problems using numerical filtering," Comm. Pure Appl. Math. (to be published, 1993).

[34]T. Beale, T. Hou, and J. Lowengrub, "Growth rates for the linear motion away from equilibrium" (in preparation).

[35]W. F. Ames, *Numerical Methods For Partial Differential Equations*, (Academic, New York, 1977).

[36]C. Anderson, "A method of local corrections for computing the velocity due to a distribution of vortex blobs," J. Comput. Phys. **62**, 111 (1986).

[37]L. Greengard and V. Rokhlin, "A fast algorithm for particle summations," J. Comput. Phys. **73**, 325 (1987).

[38]G. Carrier, M. Krook, and C. Pearson, *Functions of a Complex Variable* (McGraw-Hill, New York, 1966).

[39]Ya. B. Zel'dovich, A. G. Istratov, N. I. Kidin, and V. B. Librovich, "Flame propagation in tubes: Hydrodynamics and stability," Combust. Sci. Technol. **24**, 1 (1980).

[40]P. Pelce and P. Clavin, "The stability of curved fronts," Europhys. Lett. **3**, 907 (1987).

[41]C. W. Park and G. M. Homsy, "The instability of long fingers in Hele–Shaw flows," Phys. Fluids A **28**, 1583 (1985).

[42]J. Nittmann and H. E. Stanley, "Tip splitting without interfacial tension and dendritic growth patterns arising from molecular anisotropy," Nature **321**, 663 (1986).

[43]T. A. Witten and L. M. Sander, "Diffusion-limited aggregation," Phys. Rev. B **27**, 5686 (1983).

[44]K. J. Maloy, J. Feder, and T. Jossang, "Viscous fingering fractals in porous media," Phys. Rev. Lett. **55**, 2688 (1985).

[45]D. Bensimon, "Stability of viscous fingering," Phys. Rev. A **33**, 1302 (1986).

[46]S. Liang, "Random walk simulations of flow in Hele–Shaw cells," Phys. Rev. A **33**, 2663 (1986).

[47]S. Tanveer (private communication).